SCIENTIFIC REPORTS

OPEN

Roles of Joule heating and spin-orbit torques in the direct current induced magnetization reversal

Received: 12 March 2018
Accepted: 14 August 2018
Published online: 28 August 2018

Dong Li[1,2], Shiwei Chen[1], Yalu Zuo[1], Jijun Yun[1], Baoshan Cui[1], Kai Wu[1], Xiaobin Guo[1], Dezheng Yang[1], Jianbo Wang[1] & Li Xi[1]

Current-induced magnetization reversal via spin-orbit torques (SOTs) has been intensively studied in heavy-metal/ferromagnetic-metal/oxide heterostructures due to its promising application in low-energy consumption logic and memory devices. Here, we systematically study the function of Joule heating and SOTs in the current-induced magnetization reversal using Pt/Co/SmO_x and Pt/Co/AlO_x structures with different perpendicular magnetic anisotropies (PMAs). The SOT-induced effective fields, anisotropy field, switching field and switching current density (J_c) are characterized using electric transport measurements based on the anomalous Hall effect and polar magneto-optical Kerr effect (MOKE). The results show that the current-generated Joule heating plays an assisted role in the reversal process by reducing switching field and enhancing SOT efficiency. The out-of-plane component of the damping-like-SOT effective field is responsible for the magnetization reversal. The obtained J_c for Pt/Co/SmO_x and Pt/Co/AlO_x structures with similar spin Hall angles and different PMAs remains roughly constant, revealing that the coherent switching model cannot fully explain the current-induced magnetization reversal. In contrast, by observing the domain wall nucleation and expansion using MOKE and comparing the damping-like-SOT effective field and switching field, we conclude that the current-induced magnetization reversal is dominated by the depinning model and J_c also immensely relies on the depinning field.

Manipulating magnetization reversal in a perpendicularly magnetized heavy metal (HM)/ferromagnetic metal (FM) structure by current-induced spin-orbit torques (SOTs) has attracted considerable attention in recent years due to its potential application in high density and low energy dissipation storages compared with the conventional spin-transfer-torque (STT) devices[1–6]. The spin Hall effect (SHE)[4,7,8] resulted from HMs with the strong spin-orbit coupling (SOC) and the interfacial Rashba effect[2,9–12] due to the inversion asymmetry of the interface or crystalline structure are considered to be the major sources that can enable spin current generation and spin accumulation when passing an in-plane charge current in HMs. Therefore, the polarized spins can exert efficient torques on the adjacent FM layer to manipulate the magnetization reversal in a commonly studied HM/FM/insulator heterostructure with perpendicular magnetic anisotropy (PMA). SOTs are divided into two components, damping-like and field-like torques, which can be obtained by measuring the corresponding effective fields that can be considered as an equivalent magnetic field[13–15]. In particular, the magnetization reversal is realized mainly depending on the damping-like effective field which is proportional to the spin Hall angles (θ_{SH}) of HMs. Here, θ_{SH} is defined as the ratio of the spin current to the charge current, which can mirror the SOT's efficiency.

At present, lots of works are concentrated on enhancing the current-induced magnetization switching efficiency and reducing the critical current density for decreasing the energy consumption of future SOT-based spintronic devices. Looking for HMs, such as Pt[4,16–18], β-Ta[3,18–24], Hf[25] and β-W[26,27] with the large θ_{SH} and/or achieving the large effective θ_{SH} based on HM/FM/HM structures in which two HM layers show opposite signs of θ_{SH}[14,28,29] were carried out more recently. Besides, some reports also reveal that θ_{SH} could be tuned by varying the thickness of HM[15,30], decorating the interface between HM and FM[16,31,32], changing the crystallinity of HM[33] and even involving oxygen in HM[34]. Most of these studies can be boiled down to strengthen the driving force for the magnetization reversal and thereby improve the switching efficiency with a lower switching current density.

[1]Key Laboratory for Magnetism and Magnetic Materials of Ministry of Education & School of Physical Science and Technology, Lanzhou University, Lanzhou, 730000, People's Republic of China. [2]Research Institute of Materials Science, Shanxi Normal University, Linfen, 041004, People's Republic of China. Correspondence and requests for materials should be addressed to L.X. (email: xili@lzu.edu.cn)

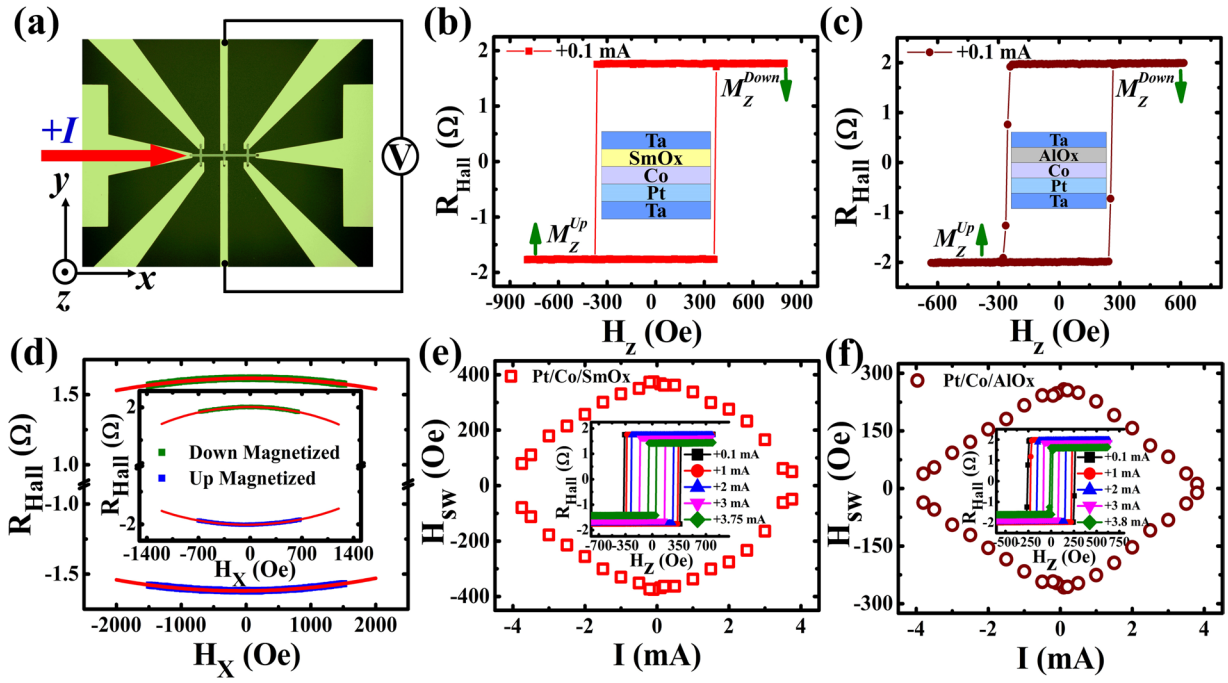

Figure 1. Device structure and anomalous Hall resistance measurements. (**a**) Optical images of the patterned Hall bar and measurement configuration. Dependence of R_{Hall} on H_z is measured at the current of +0.1 mA for Pt/Co/SmO$_x$ (**b**) and Pt/Co/AlO$_x$ (**c**) stacks. (**d**) R_{Hall} versus H_x for Pt/Co/SmO$_x$ and the inset for Pt/Co/AlO$_x$. The solid blue and green symbols correspond to "up" and "down" magnetized states, respectively. Red solid lines are the fitted curves. Switching phase diagram where H_{sw} varies against I for Pt/Co/SmO$_x$ (**e**) and Pt/Co/AlO$_x$ (**f**) stacks and the insets of them show the variation of R_{Hall}-H_z loops at different currents.

However, the obstruction term should also be taken into consideration. For instance, Liu *et al.*[4] reported that the anisotropy field needs to be overcome in the current-induced magnetization reversal based on a macrospin model at 0 K. Other reports[35–37] showed that the depinning field is an essential parameter based on a domain wall (DW) depinning model. As a consequence, it is imperative to investigate the obstruction terms in the switching and understand the switching mechanism as well as corresponding influencing factors. Especially, when a current passing through the metal layers, the simultaneously generated Joule heating may elevate the sample temperature and consequently has an influence on the magnetic properties of devices. For example, Joule heating can give rise to the reduction of the critical depinning field, which has been widely reported by the theoretical simulation and/or experimental measurement[38–40] in STT-based devices. However, the influences of Joule heating on the depinning field and current-induced magnetization reversal in SOT-based devices were rarely reported and usually ignored[41,42].

In this work, we investigate the roles of Joule heating and SOTs played in the current-induced magnetization reversal using Pt/Co/SmO$_x$ and Pt/Co/AlO$_x$ structures with different PMAs. The results show that the large direct current (dc) can dramatically decrease the depinning field (i.e. switching field) due to the current-induced Joule heating effect. However, when applying a periodic pulse current with a small duty ratio to eliminate the Joule heating effect, we find that the effect of the current-induced SOTs on the switching field is weak. More importantly, the obtained switching current density (J_c) remains roughly constant for Pt/Co/SmO$_x$ and Pt/Co/AlO$_x$ structures with quite different PMAs and nearly similar SOTs, revealing that the coherent switching model cannot fully explain the reversal behavior in the current-induced magnetization reversal process. In contrast, the switching mechanism could be the DW nucleation and expansion based on a depinning model. When the out-of-plane component of the damping-like SOT induced effective field overcomes the pinning field, a full magnetization reversal is realized. Therefore, J_c not only depends on the damping-like SOT induced effective field, but also on the depinning field. In addition, the current-induced Joule heating, which behaves like the temperature, plays an assisted role in the magnetization reversal by decreasing depinning field and increasing SOT efficiency.

Results

The anomalous Hall resistance measurements. Figure 1(a) schematically shows the patterned Hall bar structure and experimental configuration in which a direct current (I) is injected into the bar along the $+x$ axis, and the voltage induced by the anomalous Hall effect (AHE) is measured along the y axis. Figure 1(b,c) show the anomalous Hall resistance (R_{Hall}) against the external magnetic field along the z axis (H_z) measured at a positive current of +0.1 mA (the current direction is illustrated in Fig. 1(a)) for Pt/Co/SmO$_x$ and Pt/Co/AlO$_x$, respectively. The square-shape-like loops demonstrate the presence of PMA. Since R_{Hall} is proportional to the perpendicular component of the magnetization (M_z) of the Co layer, the magnetization direction M_Z^{up} (M_Z^{down}) corresponding to $R_{Hall} < 0$ ($R_{Hall} > 0$) can be identified in our experiment, which is labeled by green arrows in Fig. 1(b,c). The

longitudinal resistance (R_{xx}) is found to be around 6300 Ω and 3500 Ω for Pt/Co/SmO_x and Pt/Co/AlO_x bars with the length around 400 μm and 200 μm, respectively. As shown in Fig. 1(d), the anisotropy fields (H_k) are determined by measuring R_{Hall} versus the in-plane magnetic field along the x axis (H_x) at a small current of +0.1 mA using the formula[43,44]:

$$R_{Hall}/R_0 = \cos[\arcsin(H_x/H_k)]. \quad (1)$$

where R_0 represents the Hall resistance when the magnetization is along the z direction. H_k is respectively estimated about 6650 ± 50 Oe and 2511 ± 11 Oe for Pt/Co/SmO_x and Pt/Co/AlO_x devices, which shows a large difference of the anisotropy field for both samples. Afterwards, we begin to investigate the dependence of the switching field (H_{sw}) on I. H_{sw} is defined as an equivalent magnetic field which can make the moment from "up" state to "down" state or from "down" state to "up" state, which can be acquired from R_{Hall}-H_z loops. H_{sw} as a function of I is displayed in Fig. 1(e,f) for Pt/Co/SmO_x and Pt/Co/AlO_x, respectively, and the insets of Fig. 1(e,f) give representative R_{Hall}-H_z loops at different I. One can see that H_{sw} decreases gradually as the current increases, which can be mainly ascribed to the increase of the Joule heating generated from direct currents (see Supplementary Material S1) instead of the current-induced damping-like-SOT effective field. Since the damping-like effective field is along the x direction and the value is not more than 15 Oe, it has almost no influence on the switching field, which will be discussed in details below.

Polar Kerr hysteresis loops and Kerr differential images at different direct currents. Next, in order to reveal the effect of the direct current on the field-induced magnetization reversal, we used the polar magneto-optical Kerr microscopy technique[45] to explore the polar Kerr hysteresis loops and Kerr differential images at different direct currents during the magnetization reversal. Figure 2(a,b) show the representative Kerr differential images at the nucleation state for Pt/Co/SmO_x and Pt/Co/AlO_x stacks, respectively. The light (deep) color in the images is defined as the "up" ("down") domain or magnetized state. We find that the preferred nucleation sites are very different for the two stacks by applying an opposite H_z along the $+z$ axis, starting from the saturated state using a large H_z along the $-z$ axis. It can be ascribed to the different distributions of the depinning field due to the defects and impurities during the fabrication. For Pt/Co/SmO_x stacks, the nucleation site is relatively concentrated, showing an uniform DW expansion. However, the nucleation site is dispersive and then the DW at every nucleation site expands and further connects with each other to realize the magnetization reversal for Pt/Co/AlO_x. Figure 2(c,d) show the polar Kerr hysteresis loops at different direct currents which were collected in the green rectangle regions displayed in Fig. 2(a,b). From Fig. 2(c,d), one can see that the loops gradually become narrow as the direct current increases for Pt/Co/SmO_x and Pt/Co/AlO_x, implying the decrease of H_{sw} with the current increasing. In Fig. 2(e,f), we summarize the I dependence of H_{sw}, which is well in agreement with that obtained using electric transport measurements based on AHE (see Fig. 1(e,f)). It means that the direct current indeed has an influence on H_{sw}.

When collecting the Kerr hysteresis loops, the images of the DW nucleation and expansion were also recorded. Figure 3(a,b) show the representative Kerr differential images of the DW nucleation and expansion at different direct currents for Pt/Co/SmO_x and Pt/Co/AlO_x, respectively. At first, an "up" domain in the saturated state appears under a large H_z (−400 Oe for Pt/Co/SmO_x and −300 Oe for Pt/Co/AlO_x). Afterwards, an opposite H_z is applied to form the opposite nucleation sites. And then these nucleation sites further expand as the H_z goes on increasing until to accomplish the magnetization reversal of the green-rectangle measured regions shown in Fig. 2(a,b). In Fig. 3(a,b), we can observe that both the nucleation field and switching field in the measured regions gradually decrease as the direct current increases for the two stacks. Particularly, the nucleation site and expansion speed evidently change at the large current, revealing that the direct current could affect the magnetization reversal by means of the DW nucleation and expansion.

The influence of Joule heating on the switching field. In order to distinguish the contributions of the Joule heating ($Q_J \propto I^2$) and current-induced SOT ($\tau \propto I$) to the field-induced magnetization reversal, we also measured the polar Kerr hysteresis loops and Kerr differential images at different temperatures (T) and pulse voltages (V_p) (see Supplementary Materials S2 and S3) to investigate the effect of the T and V_p on H_{sw}. In Fig. 4(a,b), we directly compare the I^2 and T dependences of the H_{sw} for Pt/Co/SmO_x and Pt/Co/AlO_x. The H_{sw}-I^2 is extracted from the polar Kerr hysteresis loops measured by varying I at room temperature (RT) (see Fig. 2(c,d)), while H_{sw}-T is at various T without any currents (see Supplementary Material S2). From Fig. 4(a,b), one can see that the different dependences of the H_{sw} on T for Pt/Co/SmO_x and Pt/Co/AlO_x, demonstrating the different domain wall nucleation and expansion behaviors (see Fig. 2(a,b)). However, the I^2 and T dependences of the H_{sw} exhibit the same variation tendency, revealing that the Joule heating from the direct current should not be negligible and has a conclusive effect on H_{sw}. A strong Joule heating effect existed in our samples may be ascribed to that the film stacks were deposited on a 500 μm thick glass substrate with the poor thermal conductivity. Torrejon *et al.*[46] reported that even though a 2 ns wide current pulse with the amplitude of 10^8 A/cm^2 passing through a 400 × 20 nm^2 FeNi nanostrip on Si substrate with the 100 nm thick SiO_2 oxide layer, it has a 327 K temperature rise compared to a 53 K temperature rise on Si substrate with a 2 nm thick native oxide layer due to the poor thermal conductivity of SiO_2 layer. In addition, we also summarize H_{sw} against V_p at different pulse periods (T_p) with the fixed pulse width (W_p) of 100 ns to study the effect of the current-induced SOT on H_{sw} by fading out the Joule heating effect, which is shown in Fig. 4(c,d) for Pt/Co/SmO_x and Pt/Co/AlO_x, respectively. It is noted that the V_p of 28.1 V (14.1 V) corresponds to the pulse current (I_p) of about 4.5 mA (4 mA) for Pt/Co/SmO_x (Pt/Co/AlO_x). When T_p = 10 μs, H_{sw} decreases weakly as V_p increases and when T_p = 100 μs even 1 ms, H_{sw} nearly keeps constant. It means that the effect of current-induced SOT on H_{sw} is rather weak compared to the influence of the temperature or Joule heating on H_{sw}. Furthermore, it is also demonstrated that the Joule heating becomes prominent as T_p

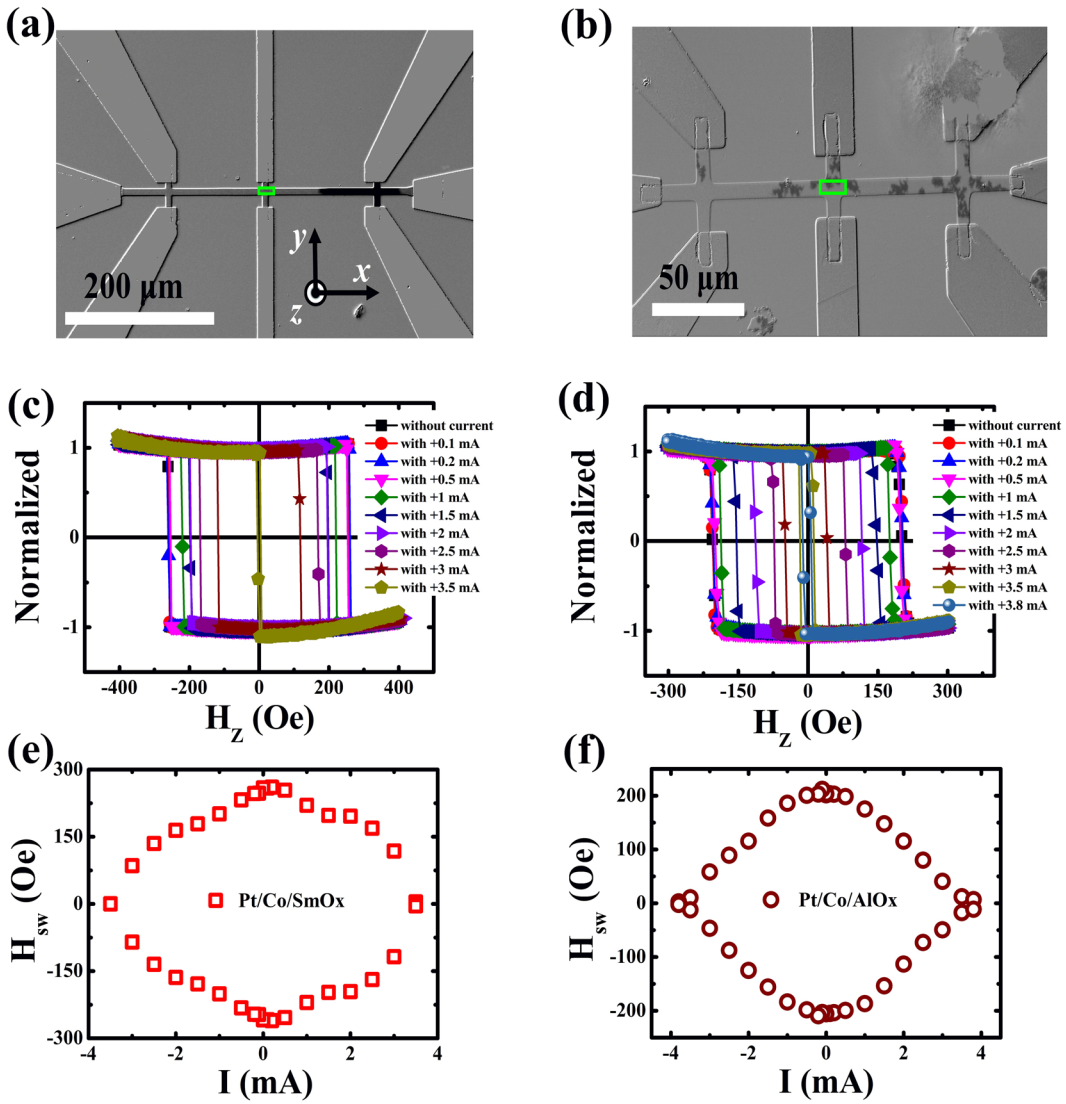

Figure 2. Polar Kerr hysteresis loops at different direct currents. Representative Kerr images for Pt/Co/SmO_x (**a**) and Pt/Co/AlO_x (**b**) during the field-induced magnetization switching, showing the differences of the DW nucleation. The light (deep) color shows the "up" ("down") domain or magnetized state. The green rectangles stand for the measured regions where polar Kerr hysteresis loops are collected. Polar Kerr hysteresis loops for Pt/Co/SmO_x (**c**) and Pt/Co/AlO_x (**d**) stacks at different direct currents. Switching phase diagram where H_{sw} varies against I for Pt/Co/SmO_x (**e**) and Pt/Co/AlO_x (**f**) stacks.

decreases or the duty ratio of W_p/T_p increases. Therefore, we can conclude that the decrease of H_{sw} with the direct current increasing should be ascribed to the increase of the direct current generated Joule heating rather than the current-induced SOT and the Joule heating like T can exert a considerable influence on H_{sw}. In order to gain more insight on the function of the Joule heating and SOT in the current-induced magnetization reversal process, we quantitatively explore the relationships between H_{sw}, SOT, and J_c, which will be described in the next part.

The harmonic Hall voltage measurements and current-induced effective fields. The current-induced damping-like and field-like effective fields were quantified by the harmonic Hall voltage measurement technique. The measurement diagrams are depicted in Fig. 5(a,b). When passing a sinusoidal current through the Hall bars along x axis, the first (V^{ω}) and second ($V^{2\omega}$) harmonic voltages were collected along y axis via an Analog-Digital (AD)/Digital-Analog (DA) data acquisition card. Therefore, the current-induced longitudinal damping-like effective field (H_{DL}) and transverse field-like effective field (H_{FL}) can be obtained by sweeping the external longitudinal magnetic field (H_L) and transverse magnetic field (H_T), respectively. And then the H_{DL} and H_{FL} are determined by the equations[19]:

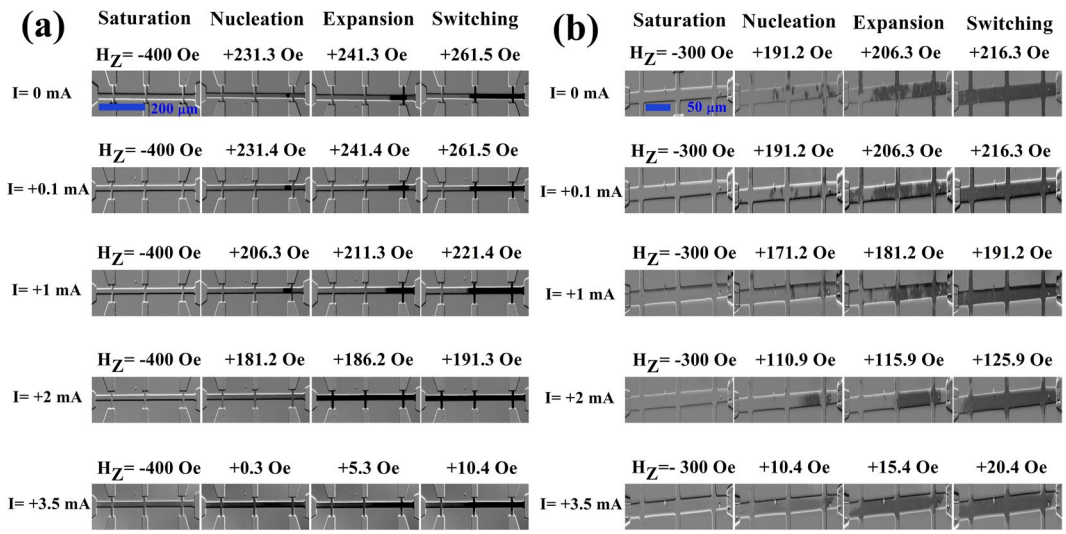

Figure 3. Kerr differential images of the DW nucleation and expansion at different direct currents. Representative Kerr images for Pt/Co/SmO_x (**a**) and Pt/Co/AlO_x (**b**) during the field-induced magnetization switching at various direct currents, showing the effect of the direct current on DW nucleation and expansion. The light (deep) color shows the "up" ("down") domain or magnetized state.

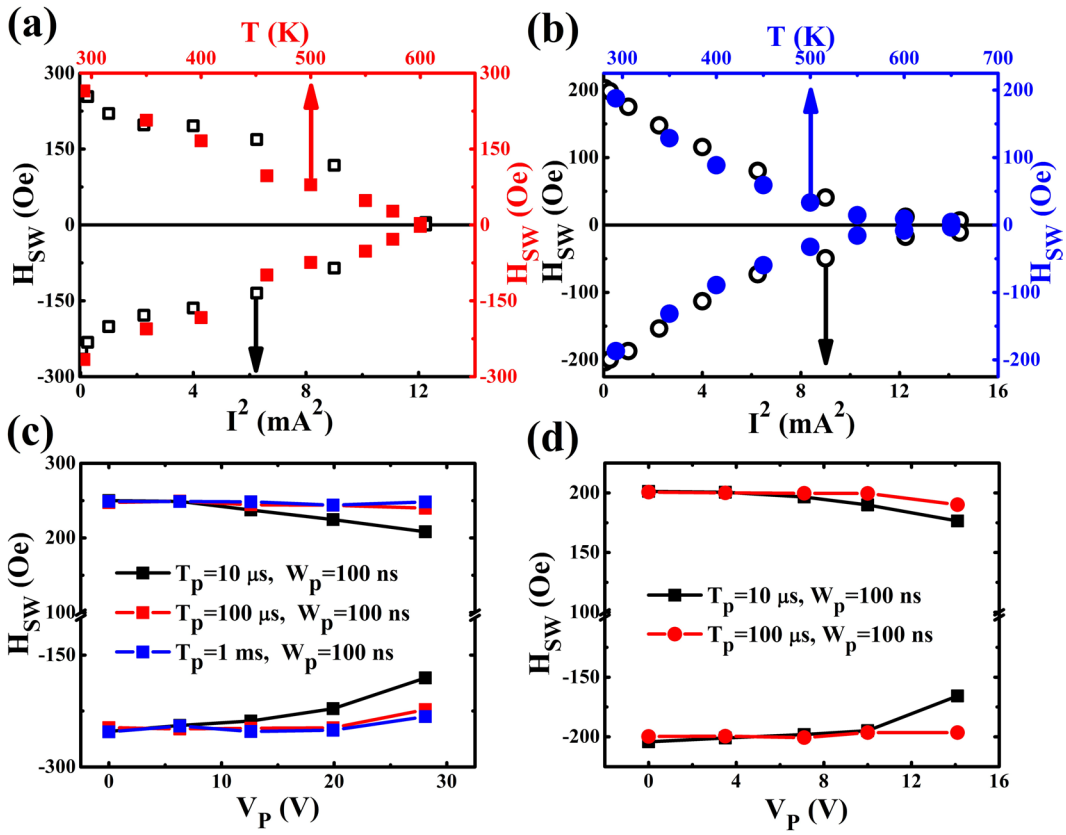

Figure 4. The direct current, temperature and pulse voltage dependences of the switching field. H_{sw} as a function of I^2 and T for Pt/Co/SmO_x (**a**) and Pt/Co/AlO_x (**b**), showing the effect of the current-induced Joule heating. H_{sw} against V_p at various T_p for Pt/Co/SmO_x (**c**) and Pt/Co/AlO_x (**d**), showing the effect of the current-induced spin-orbit torques.

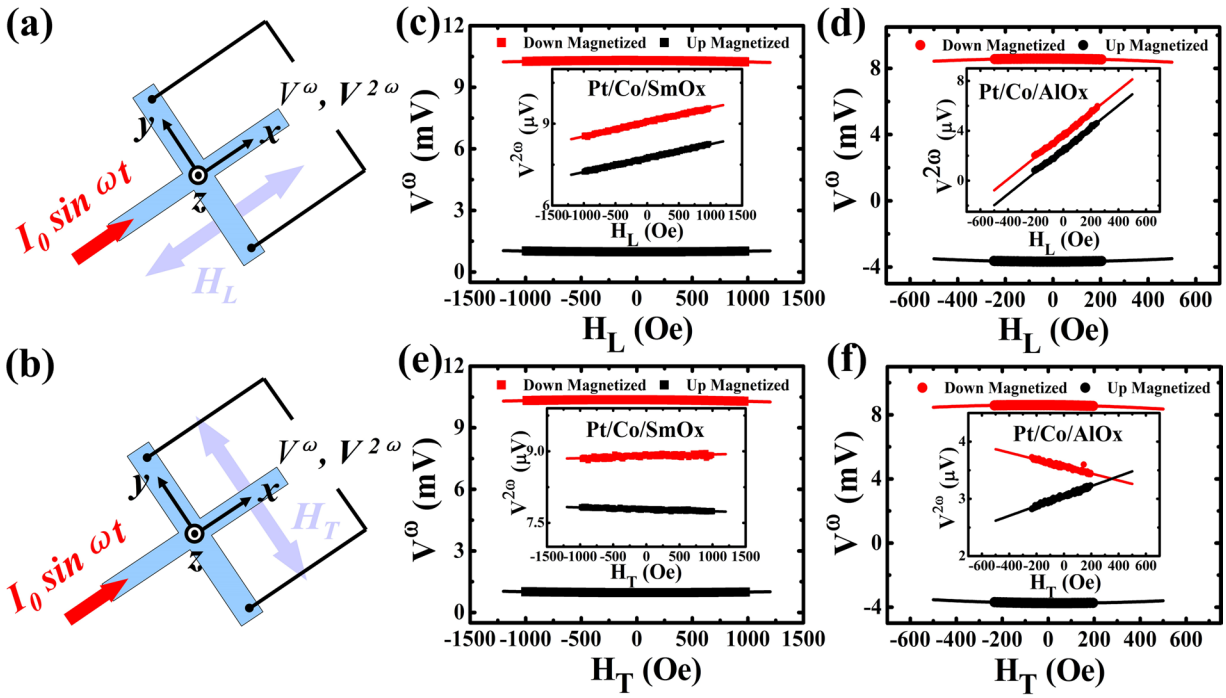

Figure 5. The harmonic Hall voltage measurements. Illustrations of the SOT-induced damping-like (**a**) and field-like (**b**) effective fields measurements. (**c–f**) V^{ω} as a function of the in-plane H_L and H_T external magnetic fields. The inset in each figure represents the $V^{2\omega}$ versus H_L and H_T. The solid black and red symbols denote "up" and "down" magnetized states, respectively and the solid lines represent the linear and quadratic fitting curves.

$$H_{DL} = -2\frac{\partial V^{2\omega}}{\partial H_L} / \frac{\partial^2 V^{\omega}}{\partial H_L^2}$$
$$H_{FL} = -2\frac{\partial V^{2\omega}}{\partial H_T} / \frac{\partial^2 V^{\omega}}{\partial H_T^2}. \quad (2)$$

Figure 5(c–f)) represent the first harmonic voltages V^{ω} as a function of H_L (H_T) for the Pt/Co/SmO_x and Pt/Co/AlO_x devices, respectively. The insets in each figure show the second harmonic voltages $V^{2\omega}$ against H_L and H_T for the corresponding devices. Furthermore, in order to calculate H_{DL} and H_{FL} according to the Eq. (2), the quadratic and linear function were used to fit the first and second harmonic curves, respectively. The results are shown in the Supplementary Material S4. It should be noted that the measured harmonic voltages generally contain the contributions resulted from both the anomalous Hall effect and planar Hall effect (PHE). Thus, a correction must be taken into consideration in Eq. (2) if these two contributions are comparable and the corrected effective fields can be expressed by[20,47–49]:

$$\Delta H_{DL(FL)} = \frac{H_{DL(FL)} \pm 2\xi H_{FL(DL)}}{1 - 4\xi^2}. \quad (3)$$

where the ± sign refers to the "up" and "down" magnetized states and ξ is the ratio of the planar Hall resistance (ΔR_{PHE}) to anomalous Hall resistance (ΔR_{AHE}). We measure the ΔR_{PHE} and ΔR_{AHE} (see Supplementary Material S4 for details about PHE measurements) and the ratio $\xi \sim 0.15$ ($\xi = \Delta R_{PHE}/\Delta R_{AHE}$) for Pt/Co/$SmO_x$ and Pt/Co/AlO_x is calculated. It means that the PHE correction is not negligible and should be considered.

The corrected damping-like effective fields (ΔH_{DL}) as a function of the amplitude (I_0) of the sinusoidal current for both devices are plotted in Fig. 6(a and c). The roughly linear dependence of the effective fields on I_0 indicates that the contributions of the non-linear effects including the current-induced Joule heating can be weak at lower currents compared to the current-induced damping-like effective fields. From the linear relationship, the damping-like SOT efficiency ($\Delta\beta_{DL}$) defined by $\Delta\beta_{DL} = \Delta H_{DL}/J_e$ (J_e is the charge current density) is found to be -3.39 ± 0.02 Oe/(10^6 A/cm^2) (3.36 ± 0.14 Oe/(10^6 A/cm^2)) for the "up" ("down") magnetized states for Pt/Co/SmO_x and -3.68 ± 0.15 Oe/(10^6 A/cm^2) (3.69 ± 0.18 Oe/(10^6 A/cm^2)) for the "up" ("down") magnetized states for Pt/Co/AlO_x. Obviously, the damping-like-SOT-induced effective fields are almost identical for two samples, which is due to the same contribution from the heavy metal Pt. Meanwhile, according to the formula[4,50,51]:

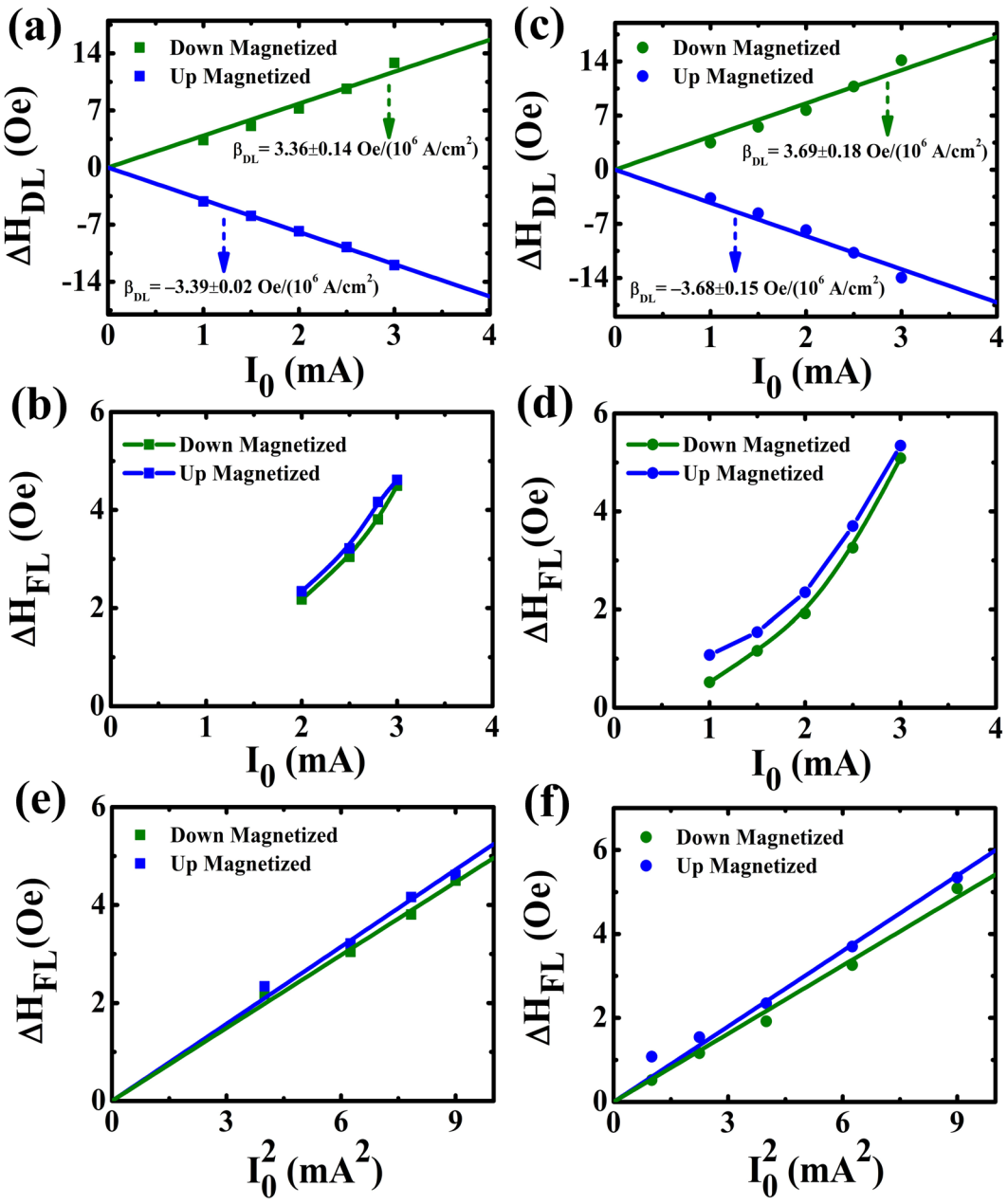

Figure 6. Current-induced effective fields after the planar Hall effect correction. (**a**–**d**) SOT-induced damping-like and field-like effective fields for Pt/Co/SmO_x (Pt/Co/AlO_x) as a function of the amplitude I_0 of the sinusoidal current. The blue and green symbols denote "up" and "down" magnetized states, respectively. The field-like effective fields against I_0^2 for Pt/Co/SmO_x (**e**) and Pt/Co/AlO_x (**f**), respectively.

$$\theta_{SH} = J_s/J_e = \left(\frac{2|e|M_s t_{FM}}{\hbar}\right)(\Delta H_{DL}/J_e). \tag{4}$$

where e is the elementary charge, M_s is the saturation magnetization of the samples which is determined to be about 1.15×10^6 A/m and 1.12×10^6 A/m at RT for Pt/Co/SmO_x and Pt/Co/AlO_x, respectively, t_{FM} is the thickness of the cobalt layer and $\hbar$ is the reduced Planck constant. We can also estimate the θ_{SH} at RT which equals to 0.071 ± 0.002 and 0.074 ± 0.004 for Pt/Co/SmO_x and Pt/Co/AlO_x, respectively, close to the previous reported value for Pt[52,53].

The corrected field-like effective fields (ΔH_{FL}) are also plotted as a function of I_0 in the same manner for both devices displayed in Fig. 6(b and d). Unlike ΔH_{DL}, a non-linear quadratic behavior of ΔH_{FL} versus I_0 is observed. It is not well in agreement with the linear dependence of the field-like effective fields on the currents reported in the references[7,54,55]. One possible explanation for the non-linear behavior is the Joule heating effect. Although the thermal effect also affects ΔH_{DL} at the same time, it seems to be weak as discussed above. It could be ascribed to

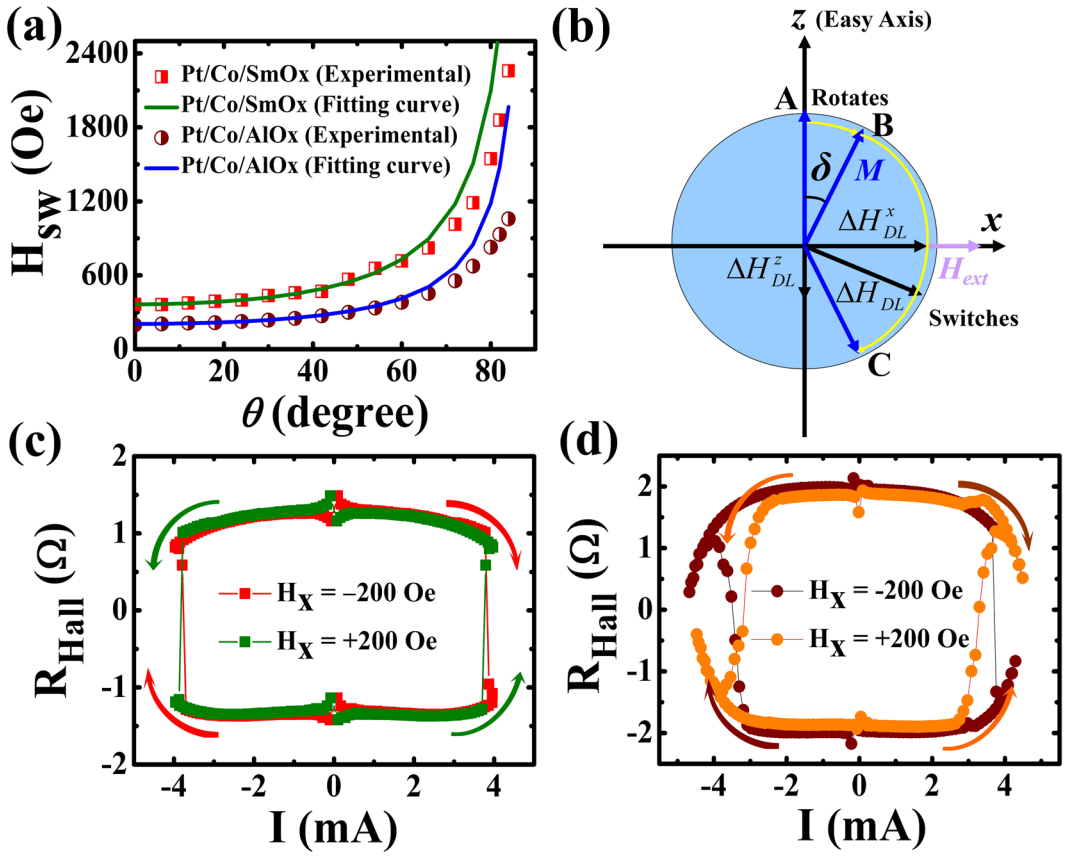

Figure 7. Current-induced magnetization reversal. (**a**) H_{sw} versus θ. θ is the angle between the z axis and H_{ext} in the x-z plane. (**b**) Schematic diagram illustrating the current-induced magnetization switching process. The perpendicular component $\Delta H_{DL}^{x} = \Delta H_{DL}\cos\delta$ of ΔH_{DL} causes a rotation of the magnetization away from the easy axis, whereas the parallel component $\Delta H_{DL}^{z} = \Delta H_{DL}\sin\delta$ is responsible for the irreversible switching. Current-induced magnetization reversal curves for Pt/Co/SmO_x (**c**) and Pt/Co/AlO_x (**d**) with an in-plane bias magnetic field of $H_x = \pm 200$ Oe.

the different temperature dependences of $\Delta H_{DL}/J_e$ and $\Delta H_{FL}/J_e$ as reported in the references[20,56,57], in which $\Delta H_{FL}/J_e$ is highly sensitive to temperature, while $\Delta H_{DL}/J_e$ shows a weak temperature dependence in Ta-based, Pt-based, and W-based samples. In order to demonstrate the effect of the Joule heating, we extract the dependence of ΔH_{FL} on I_0^2 shown in Fig. 6(e,f) for Pt/Co/SmO_x and Pt/Co/AlO_x, respectively. From Fig. 6(e,f), one can see that the ΔH_{FL} varies linearly with I_0^2, implying that the contribution of the Joule heating cannot be negligible compared to the current-induced field-like effective fields from SHE or interfacial Rashba effect.

Discussion

Combining the variation of the H_{sw} and ΔH_{DL} at different currents, we discuss the roles of the Joule heating and spin-orbit torque played in the current-induced magnetization reversal process. In Fig. 7(a), we characterize H_{sw}-θ curves (θ is defined as the angle between the external magnetic field and z axis in the x-z plane) obtained from the angle dependent R_{Hall}-H_z loops which are measured at $I = 0.1$ mA to eliminate the influence of the SOTs and Joule heating. From Fig. 7(a), one can see that H_{sw} follows an inverse cosθ relationship at small angles as shown in solid lines. It indicates that the magnetization reversal is dominated by the DW depinning in the large anisotropic systems ($H_{sw} \ll H_k$)[36,58,59] when the external magnetic field deviates from the z axis in a small angle range. Figure 7(b) describes the schematic diagram of the current-induced magnetization reversal process. We assume that the magnetic moment vector ($\boldsymbol{M}$) is rotated from A to B and deviates a small angle (δ) away from the z axis (easy axis) when applying an in-plane bias magnetic field (H_{ext}). According to the equation which is expressed as $\Delta \boldsymbol{H}_{DL} = \Delta H_{DL}(\boldsymbol{\sigma} \times \boldsymbol{m})$[60], where $\boldsymbol{m}$ and $\boldsymbol{\sigma}$ are the unit vector along the magnetization and spin polarization unit vector, respectively, the damping-like SOT induced effective field vector ($\Delta \boldsymbol{H}_{DL}$) can be resolved into the perpendicular component ($\Delta \boldsymbol{H}_{DL}^{x}$) and parallel component ($\Delta \boldsymbol{H}_{DL}^{z}$). Here, ΔH_{DL} parameterizes the effective field, which can be written as $\Delta H_{DL} = \hbar\theta_{SH}J_e/2|e|M_s t_{FM}$. Thus, the $\Delta H_{DL}^{x} = \Delta H_{DL}\cos\delta$ can further cause a rotation of the magnetization away from the easy axis, whereas the $\Delta H_{DL}^{z} = \Delta H_{DL}\sin\delta$ is responsible for the irreversible magnetization reversal. Especially, $\boldsymbol{M}$ is switched from B to C when ΔH_{DL}^{z} overcomes the depinning field.

Figure 7(c,d) show the current-induced magnetization reversal curves under an in-plane bias magnetic field of $H_x = \pm 200$ Oe for Pt/Co/SmO_x and Pt/Co/AlO_x, respectively. According to M_Z^{up} (M_Z^{down}) corresponding to $R_{Hall} < 0$ ($R_{Hall} > 0$) in our experiment, the directions of the current and assisted H_x co-determine the polarity of

the magnetization reversal. In addition, the critical switching current (I_c) under the bias field of $H_x = \pm 200$ Oe is around 3.8 and 3.7 mA that correspond to the J_c of 4.4×10^6 and 4.3×10^6 A/cm^2 for Pt/Co/SmO_x and Pt/Co/AlO_x, respectively, assuming that the current uniformly flows across metallic layers. Since the magnitude of $\Delta\beta_{DL}$ for both samples is ~3.5 Oe per 10^6 Acm^{-2} at RT as discussed above (see Supplementary Material S5 about $\Delta\beta_{DL}$ against T) and J_c is ~4.35×10^6 Acm^{-2} for Pt/Co/SmO_x and Pt/Co/AlO_x, the ΔH_{DL} is ~15 Oe and $\Delta H_{DL}^z = \Delta H_{DL}\sin\delta$ may be more small at the critical switching process. Therefore, the $\boldsymbol{M}$ cannot have a switching only depending on the damping-like effective field. The current-induced magnetization reversal should be also on the basis of the contribution that the Joule heating from the current makes the H_{sw} decrease to a small value. That is, Joule heating plays an assisted role in the current-induced magnetization reversal and the out-of-plane component of ΔH_{DL} should be regarded as the effective driving force in overcoming the H_{sw}. In addition, the results show that J_c remains roughly equivalent for Pt/Co/SmO_x and Pt/Co/AlO_x structures with similar spin Hall angles and different magnetic anisotropies, which can be also explained by that H_{sw} of the two stacks is reduced to a close value due to the Joule heating effect when the current reaches to I_c. Finally, the weak T dependent H_k (see the Supplementary Material S5) has also demonstrated that H_k has no substantial influence on the depinning mechanism with the existence of Joule heating. Whereas, the tendency of H_{sw} varying versus I or T may be related to H_k in the thermal assisted magnetization reversal. Besides, the T dependent M_s and $\Delta\beta_{DL}$ (see the Supplementary Material S5) reveal that the current-generated Joule heating can also enhance SOT efficiency like T.

Based on above discussions, it also gives us some enlightenment on the current induced field-free magnetization reversal. On one hand, ΔH_{DL} is along the x axis ($\delta = 0$) without an in-plane bias field H_{ext}. When increasing the current, the ΔH_{DL} is also increasing, which can make $\boldsymbol{M}$ rotating away from z axis ($\delta > 0$). $\Delta H_{DL}^z = \Delta H_{DL}\sin\delta$ which is responsible for the irreversible switching yields at the same time. On the other hand, the Joule heating is gradually predominant as the current increases, which can dramatically decrease the H_{sw}. Therefore, $\boldsymbol{M}$ can be switched when the competition of ΔH_{DL}^z and H_{sw} is comparable at a certain current without the assistance of an in-plane bias field. However, the larger switching current induced thermal fluctuation may destroy the thermal stability of devices and even the devices may be burned at the large current. It is essential to choose the materials and structures with the larger PMA and/or θ_{SH}, because the former can resist the thermal fluctuation from Joule heating and the latter can reduce the switching current and Joule heating.

Conclusions

In summary, we have investigated the roles of the Joule heating and current-induced spin-orbit torque played in the current-induced magnetization reversal in Pt/Co/SmO_x and Pt/Co/AlO_x structures with different perpendicular magnetic anisotropies. The results show that the Joule heating generated from the direct current plays an assisted role in the switching process since it dramatically decreases the switching field and enhances the SOT efficiency. The out-of-plane component of the damping-like-SOT effective field is the real effective field which drives magnetic moments switching. When the Joule heating makes the switching field reduce to a critical threshold that the effective field can overcome, the magnetization realizes a full reversal. Moreover, the switching current density shows no prominent difference for Pt/Co/SmO_x and Pt/Co/AlO_x structures with similar spin Hall angles and different magnetic anisotropies, implying that the coherent switching model cannot fully explain the current-induced magnetization reversal. Nevertheless, by observing the domain wall nucleation and expansion during the field-induced magnetization reversal, we conclude that the depinning model should be dominant and the switching current density also relies on the switching field (i.e. depinning field) which can be greatly affected by Joule heating. The observed non-linear current dependence of the field-like-SOT effective field in both structures may be also affected by Joule heating. These findings could provide a legible picture of the SOT-induced magnetization reversal and highlight the assistant role of the current-generated Joule heating, which is conducive to understand and manipulate current-induced magnetization reversal in SOT-based spintronic devices.

Methods

Sample preparation. The stacks with the structures of Ta(3)/Pt(5)/Co(0.6)/SmO_x(1)/Ta(3) and Ta(3)/Pt(5)/Co(0.6)/AlO_x(0.5)/Ta(3) (thickness in nm) were deposited on corning glass substrates with the thickness of 500 μm by direct current (dc) magnetron sputtering. The growth was carried out at room temperature with a base pressure below 4.0×10^{-5} Pa. Among the samples, the bottom 3 nm Ta is used as the seed layer to enhance the PMA and the top 3 nm Ta as capping layer in order to prevent degradation of the oxide layers due to air exposure and the annealing. The thin film stacks were patterned into Hall bars with the width of 8.5 μm using standard photo-lithography and Ar-ion milling. The Hall bars were connected by Ta(20 nm)/Pt(30 nm) electrode pads. Afterwards, the devices were annealed at 400 °C for 1 h with a background pressure of 3.0×10^{-4} Pa to obtain the PMA.

Measurement setup. The anomalous Hall resistances were measured using the electric transport measurements with a Keithley 6221 current source for injecting a DC current into the Hall bar along the x axis and a 2182 nano-voltmeter for collecting the Hall voltage across the bar along the y axis (Fig. 1(a)). The harmonic Hall voltage measurements were carried out using a sinusoidal current with a frequency of 133 Hz generated by the Keithley 6221 current source and the harmonic voltages were collected using an Analog-Digital (AD)/Digital-Analog (DA) data acquisition card. The saturation magnetization and planar Hall resistance were determined with a physical property measurement system (PPMS). A polar magneto-optical Kerr microscope was used to record the polar Kerr hysteresis loops and Kerr differential images of the domain wall nucleation and expansion during the field-induced magnetization switching. In order to obtain the Kerr differential images, the film was firstly saturated in one direction using a large out-of-plane magnetic field and then the saturated domain was chose as the background. After subtracting the background, the nucleated domain in differential modes

appeared by applying a reverse magnetic field. The cross region in the middle of the Hall bar (Fig. 2(a,b)) was served as the measured area to collect the Kerr hysteresis loops and determine the switching field.

Data Availability. The datasets generated during the current study are available from the corresponding author on reasonable request.

References

1. Mangin, S. *et al*. Current-induced magnetization reversal in nanopillars with perpendicular anisotropy. *Nat. Mater.* **5**, 210 (2006).
2. Miron, I. M. *et al*. Perpendicular switching of a single ferromagnetic layer induced by in-plane current injection. *Nature* **476**, 189 (2011).
3. Liu, L. *et al*. Spin-torque switching with the giant spin Hall effect of tantalum. *Science* **336**, 555 (2012).
4. Liu, L. *et al*. Current-induced switching of perpendicularly magnetized magnetic layers using spin torque from the spin Hall effect. *Phys. Rev. Lett.* **109**, 096602 (2012).
5. Jungwirth, T., Wunderlich, J. & Olejnik, K. Spin Hall effect devices. *Nat. Mater.* **11**, 382 (2012).
6. Torrejon, J. *et al*. Current-driven asymmetric magnetization switching in perpendicularly magnetized CoFeB/MgO heterostructures. *Phys. Rev. B* **91**, 214434 (2015).
7. Emori, S. *et al*. Current-driven dynamics of chiral ferromagnetic domain walls. *Nat. Mater.* **12**, 611 (2013).
8. Haazen, P. P. J. *et al*. Domain wall depinning governed by the spin Hall effect. *Nat. Mater.* **12**, 299 (2013).
9. Miron, I. M. *et al*. Current-driven spin torque induced by the Rashba effect in a ferromagnetic metal layer. *Nat. Mater.* **9**, 230 (2010).
10. Kim, K. W. *et al*. Magnetization dynamics induced by in-plane currents in ultrathin magnetic nanostructures with Rashba spin-orbit coupling. *Phys. Rev. B* **85**, 180404 (2012).
11. Qiu, X. *et al*. Spin-orbit-torque engineering via oxygen manipulation. *Nat. Nanotechnol.* **10**, 333 (2015).
12. Tiwari, D. *et al*. Antidamping spin-orbit torques in epitaxial-Py(100)/β-Ta. *Appl. Phys. Lett.* **111**, 232407 (2017).
13. Slonczewski, J. C. Currents and torques in metallic magnetic multilayers. *J. Magn. Magn. Mater.* **247**, 324 (2002).
14. Woo, S. *et al*. Enhanced spin-orbit torques in Pt/Co/Ta heterostructures. *Appl. Phys. Lett.* **105**, 212404 (2014).
15. Allen, G. *et al*. Experimental demonstration of the coexistence of spin Hall and Rashba effects in β-tantalum/ferromagnet bilayers. *Phys. Rev. B* **91**, 144412 (2015).
16. Zhang, W. F. *et al*. Role of transparency of platinum-ferromagnet interfaces in determining the intrinsic magnitude of the spin Hall effect. *Nat. Phys.* **11**, 496 (2015).
17. Nguyen, M. H., Ralph, D. C. & Buhrman, R. A. Spin torque study of the spin Hall conductivity and spin diffusion length in platinum thin films with varying resistivity. *Phys. Rev. Lett.* **116**, 126601 (2016).
18. Vélez, S. *et al*. Hanle magnetoresistance in thin metal films with strong spin-orbit coupling. *Phys. Rev. Lett.* **116**, 016603 (2016).
19. Kim, J. *et al*. Layer thickness dependence of the current-induced effective field vector in Ta|CoFeB|MgO. *Nat. Mater.* **12**, 240 (2013).
20. Qiu, X. *et al*. Angular and temperature dependence of current induced spin-orbit effective fields in Ta/CoFeB/MgO nanowires. *Sci. Rep.* **4**, 4491 (2014).
21. Yu, G. Q. *et al*. Magnetization switching through spin-Hall-effect-induced chiral domain wall propagation. *Phys. Rev. B* **89**, 104421 (2014).
22. Wu, D. *et al*. In-plane current-driven spin-orbit torque switching in perpendicularly magnetized films with enhanced thermal tolerance. *Appl. Phys. Lett.* **108**, 212406 (2016).
23. Avci, C. O. *et al*. Fieldlike and antidamping spin-orbit torques in as-grown and annealed Ta/CoFeB/MgO layers. *Phys. Rev. B* **89**, 214419 (2014).
24. Zhang, C. *et al*. Spin-orbit torque induced magnetization switching in nanoscale Ta/CoFeB/MgO. *Appl. Phys. Lett.* **107**, 012401 (2015).
25. Ramaswamy, R. *et al*. Hf thickness dependence of spin-orbit torques in Hf/CoFeB/MgO heterostructures. *Appl. Phys. Lett.* **108**, 202406 (2016).
26. Pai, C. F. *et al*. Spin transfer torque devices utilizing the giant spin Hall effect of tungsten. *Appl. Phys. Lett.* **101**, 122404 (2012).
27. Hao, Q. & Xiao, G. Giant spin Hall effect and switching induced by spin-transfer torque in a W/$Co_{40}Fe_{40}B_{20}$/MgO structure with perpendicular magnetic anisotropy. *Phys. Rev. Appl.* **3**, 034009 (2015).
28. Yu, J. W. *et al*. Large spin-orbit torques in Pt/Co-Ni/W heterostructures. *Appl. Phys. Lett.* **109**, 042403 (2016).
29. Ueda, K. *et al*. Effect of rare earth metal on the spin-orbit torque in magnetic heterostructures. *Appl. Phys. Lett.* **108**, 232405 (2016).
30. Behera, N., Chaudhary, S. & Pandya, D. K. Anomalous anti-damping in sputtered β-Ta/Py bilayer system. *Sci. Rep.* **6**, 19488 (2016).
31. Nan, T. X. *et al*. Comparison of spin-orbit torques and spin pumping across NiFe/Pt and NiFe/Cu/Pt interfaces. *Phys. Rev. B* **91**, 214416 (2015).
32. Cui, B. S. *et al*. Current-induced magnetization switching in Pt/Co/Ta with interfacial decoration by insertion of Cr to enhance perpendicular magnetic anisotropy and spin-orbit torques. *Appl. Phys. Express* **11**, 013001 (2018).
33. Zhang, W. *et al*. All-electrical manipulation of magnetization dynamics in a ferromagnet by antiferromagnets with anisotropic spin Hall effects. *Phys. Rev. B* **92**, 144405 (2015).
34. Demasius, K. U. *et al*. Enhanced spin-orbit torques by oxygen incorporation in tungsten films. *Nat. Commun.* **7**, 10644 (2016).
35. Huang, B. C. *et al*. Thermally assisted magnetic switching of a single perpendicularly magnetized layer induced by an in-plane current. *Appl. Phys. Lett.* **105**, 022407 (2014).
36. Lee, O. J. *et al*. Central role of domain wall depinning for perpendicular magnetization switching driven by spin torque from the spin Hall effect. *Phys. Rev. B* **89**, 024418 (2014).
37. Cao, J. W. *et al*. Spin orbit torques induced magnetization reversal through asymmetric domain wall propagation in Ta/CoFeB/MgO structures. *Sci. Rep.* **8**, 1355 (2018).
38. Yamaguchi, A. *et al*. Reduction of threshold current density for current-driven domain wall motion using shape control. *Jpn. J. Appl. Phys.* **45**, 3850 (2006).
39. Yamaguchi, A. *et al*. Effect of Joule heating in current-driven domain wall motion. *Appl. Phys. Lett.* **86**, 012511 (2005).
40. Moretti, S., Raposo, V. & Martinez, E. Influence of Joule heating on current-induced domain wall depinning. *J. Appl. Phys.* **119**, 213902 (2016).
41. Zhao, Z. Y. *et al*. Spin Hall switching of the magnetization in Ta/TbFeCo structures with bulk perpendicular anisotropy. *Appl. Phys. Lett.* **106**, 132404 (2015).
42. Fukami, S. *et al*. Magnetization switching by spin-orbit torque in an antiferromagnet-ferromagnet bilayer system. *Nat. Mater.* **15**, 535 (2016).
43. Zhang, C. *et al*. Critical role of W deposition condition on spin-orbit torque induced magnetization switching in nanoscale W/CoFeB/MgO. *Appl. Phys. Lett.* **109**, 192405 (2016).
44. Emori, S. *et al*. Large voltage-induced modification of spin-orbit torques in Pt/Co/GdO_x. *Appl. Phys. Lett.* **105**, 222401 (2014).
45. Hubert, A. & Schäfer, R. Magnetic domains: the analysis of magnetic microstructures (Springer, 1998).
46. Torrejon, J. *et al*. Unidirectional thermal effects in current-induced domain wall motion. *Phys. Rev. Lett.* **109**, 106601 (2012).
47. Hayashi, M. *et al*. Quantitative characterization of the spin-orbit torque using harmonic Hall voltage measurements. *Phys. Rev. B* **89**, 144425 (2014).

48. Garello, K. *et al*. Symmetry and magnitude of spin-orbit torques in ferromagnetic heterostructures. *Nat. Nanotechnol.* **8**, 587 (2013).
49. Gabor, M. S. *et al*. Spin-orbit torques and magnetization switching in W/Co_2FeAl/MgO structures. *J. Phys. D: Appl. Phys.* **49**, 365003 (2016).
50. Khvalkovskiy, A. V. *et al*. Matching domain-wall configuration and spin-orbit torques for efficient domain-wall motion. *Phys. Rev. B* **87**, 020402 (R) (2013).
51. Hao, Q. & Xiao, G. Giant spin Hall effect and magnetotransport in a Ta/CoFeB/MgO layered structure: A temperature dependence study. *Phys. Rev. B* **91**, 224413 (2015).
52. Razavi, S. A. *et al*. Joule heating effect on field-free magnetization switching by spin-orbit torque in exchange-biased systems. *Phys. Rev. Appl.* **7**, 024023 (2017).
53. Rojas-Sánchez, J. C. *et al*. Spin pumping and inverse spin Hall effect in platinum: The essential role of spin-memory loss at metallic interfaces. *Phys. Rev. Lett.* **112**, 106602 (2014).
54. Akyol, M. *et al*. Effect of the oxide layer on current-induced spin-orbit torques in Hf|CoFeB|MgO and Hf|CoFeB|TaO_x structures. *Appl. Phys. Lett.* **106**, 032406 (2015).
55. Wu, D. *et al*. Spin-orbit torques in perpendicularly magnetized $Ir_{22}Mn_{78}$/$Co_{20}Fe_{60}B_{20}$/MgO multilayer. *Appl. Phys. Lett.* **109**, 222401 (2016).
56. Kim, J. *et al*. Anomalous temperature dependence of current-induced torques in CoFeB/MgO heterostructures with Ta-based underlayers. *Phys. Rev. B* **89**, 174424 (2014).
57. Ou, Y. X. *et al*. Origin of fieldlike spin-orbit torques in heavy metal/ferromagnet/oxide thin film heterostructures. *Phys. Rev. B* **94**, 140414 (R) (2016).
58. Schumacher, F. On the modification of the Kondorsky function. *J. Appl. Phys.* **70**, 3184 (1991).
59. Singh, A. *et al*. Mechanism of coercivity in epitaxial $SmCo_5$ thin films. *Phys. Rev. B* **77**, 104443 (2008).
60. Yu, G. Q. *et al*. Switching of perpendicular magnetization by spin-orbit torques in the absence of external magnetic fields. *Nat. Nanotechnol.* **9**, 548 (2014).

Acknowledgements

This work was supported by the National Natural Science Foundation of China (No. 51671098), the Natural Science Foundation of Gansu Province (No. 145RJZA154), the Program for Changjiang Scholars and Innovative Research Team in University PCSIRT (No. IRT16R35), and the Fundamental Research Funds for Central Universities (lzujbky-2015-122).

Author Contributions

D.L. and L.X. conceived the experiments. D.L., J.Y., K.W., X.G. and B.C. fabricated the device. D.L. and S.C. conducted the electrical measurements. D.L., Y.Z., D.Y., J.W. and L.X. discussed the results. D.L. and L.X. wrote and revised this manuscript. All authors read and approved the final manuscript.

Additional Information

Supplementary information accompanies this paper at https://doi.org/10.1038/s41598-018-31201-2.

Competing Interests: The authors declare no competing interests.

Publisher's note: Springer Nature remains neutral with regard to jurisdictional claims in published maps and institutional affiliations.